RSC Advances

PAPER

View Article Online
View Journal | View Issue

Cite this: *RSC Adv.*, 2023, **13**, 1516

Computational insight into a mechanistic overview of water exchange kinetics and thermodynamic stabilities of bis and tris-aquated complexes of lanthanides†

Niharika Keot and Manabendra Sarma *

A thorough investigation of Ln^{3+} complexes with more than one inner-sphere water molecule is crucial for designing high relaxivity contrast agents (CAs) used in magnetic resonance imaging (MRI). This study accomplished a comparative stability analysis of two hexadentate (H_3cbda and H_3dpaa) and two heptadentate (H_4peada and H_3tpaa) ligands with Ln^{3+} ions. The higher stability of the hexadentate H_3cbda and heptadentate H_4peada ligands has been confirmed by the binding affinity and Gibbs free energy analysis in aqueous solution. In addition, energy decomposition analysis (EDA) reveals the higher binding affinity of the $peada^{4-}$ ligand than the $cbda^{3-}$ ligand towards Ln^{3+} ions due to the higher charge density of the $peada^{4-}$ ligand. Moreover, a mechanistic overview of water exchange kinetics has been carried out based on the strength of the metal–water bond. The strength of the metal–water bond follows the trend Gd–O47 (w) > Gd–O39 (w) > Gd–O36 (w) in the case of the tris-aquated $[Gd(cbda)(H_2O)_3]$ and Gd–O43 (w) > Gd–O40 (w) for the bis-aquated $[Gd(peada)(H_2O)_2]^-$ complex, which was confirmed by bond length, electron density (ρ), and electron localization function (ELF) at the corresponding bond critical points. Our analysis also predicts that the activation energy barrier decreases with the decrease in bond strength; hence k_{ex} increases. The ^{17}O and ^{1}H hyperfine coupling constant values of all the coordinated water molecules were different, calculated by using the second-order Douglas–Kroll–Hess (DKH2) approach. Furthermore, the ionic nature of the bonding in the metal–ligand (M–L) bond was confirmed by the Quantum Theory of Atoms-In-Molecules (QTAIM) and ELF along with energy decomposition analysis (EDA). We hope that the results can be used as a basis for the design of highly efficient Gd(III)-based high relaxivity MRI contrast agents for medical applications.

Received 15th September 2022
Accepted 8th December 2022

DOI: 10.1039/d2ra05810c

rsc.li/rsc-advances

1 Introduction

The chemistry of lanthanide complexes in aqueous solution has been considered one of the prominent research areas due to their fruitful implementation in diagnostics and therapy.[1–5] This includes the luminescent lanthanide complexes (specifically Eu^{3+} and Tb^{3+}) used in bioanalytical and optical imaging,[6–8] and radioisotopes of lanthanides (^{177}Lu) used in radioimmunotherapy.[9] Indeed, Gd^{3+} complexes attract considerable interest since they are commonly used as contrast agents in magnetic resonance imaging (MRI).[10] Though MRI has tremendous medical applications, one of the major challenges is its relatively low sensitivity.[11,12] To increase the sensitivity, an additional agent called an MRI contrast agent (CA) is required, which alters the properties of nearby water protons after addition.[13] The capability or sensitivity of a contrast agent is exhibited through its relaxivity (r). Relaxivity can be defined as the paramagnetic magnification of the relaxation rate of the water proton, which is directly proportional to the concentrations of the CAs used.[14,15]

The most important MRI contrast agents are metal-based paramagnetic ions.[10,16] In contrast to other metal ions, discrete Gd^{3+}-based complexes are widely used as clinical paramagnetic contrast agents. This is because of their large number of unpaired electrons and slow electronic relaxation.[17,18] However, the toxicity profile of Gd^{3+} ions is very high. A large or repeated dose of them causes nephrogenic systemic fibrosis (NSF) in patients with renal disorder.[19] The food and drug administration (FDA) has placed restrictions on the application of Gd^{3+}-based contrast agents (GBCs) due to the revelation of the connection between Gd^{3+} and NSF.[20,21]

The current concerns of researchers are about the safety of MRI contrast agents and designing new contrast agents with

Department of Chemistry, Indian Institute of Technology Guwahati, Assam, 781039, India. E-mail: msarma@iitg.ac.in; Tel: +91 361 2582318

† Electronic supplementary information (ESI) available: Bond length and binding energy values, optimized geometries of the complexes, relaxed potential energy surface scan, intrinsic reaction coordinate, electron density, ELF and Laplacian values, and Cartesian coordinates of the complexes. See DOI: https://doi.org/10.1039/d2ra05810c

enhanced thermodynamic stability and kinetic inertness.[22,23] This can be achieved by complexation of the metal ion with ligands that prevent the release of the free Gd(III) ion. Based on the toxicity profile, many research groups focus on developing a contrast agent with high relaxivity so that a lower dose can be administered.[24–26] Among the various factors, water exchange of the coordinated water molecules with the bulk water is one of the important tools to be optimized for higher relaxivity of MRI CAs. Various research groups[27–30] have also focused on designing CAs with more than one inner-sphere water molecule to improve relaxivity. It is well established that, indifferent to the field strength, relaxivity increases proportionally to the number of coordinated water molecules (q).[31] Merbach *et al.*[32,33] first considered the whole lanthanide series to study the water exchange rate (k_{ex}). Despite the significance of optimizing the water exchange to get an efficient MRI contrast agent, this issue is ignored in the literature. As far as the authors are aware, only limited studies have been done until now.[34–37] The water exchange rate of the inner-sphere water molecules has been accelerated by factors such as increasing the overall compound negative charge and the steric hindrance surrounding the water molecules.[38] Clinically approved CAs contain only a single molecule of water in the inner coordination sphere.[34] The water exchange rates and structural elucidation of the most studied chelators 1,4,7,10-tetraaza-1,4,7,10-tetrakis(carboxymethyl) cyclododecane(DOTA)[39,40] and diethylenetriaminepentaacetic acid (DTPA)[41] have been well established. However, for $q > 1$ complexes, *i.e.* $[Ln(L)(H_2O)_{2-3}]^x$ [L = ligand, x = charge, Ln = La^{3+} to Lu^{3+}], no such systematic explanation of the water exchange and structural analysis has been done so far.[27,42,43] Indeed, with an increase in the number of inner-sphere water molecules, the ligand's denticity reduces, which may reduce the complexes' thermodynamic stability.[34]

A few Gd(III) chelates with $q > 1$ have been reported. One such system is the Gd(III) complex of a pyridine-containing macrocyclic ligand with two acetic acids and one methylenephosphonic arm (PCP2A),[44,45] but further functionalization of this complex was found to be difficult. Another class of complexes with a higher hydration number ($q > 1$) is represented by tris-bidentate Gd(III)-hydroxypyridinone (HOPO) based derivatives, which are presently under strong scrutiny.[46] Previously, Bretonnière *et al.* synthesized a ligand α,α′,α″-nitrilotri(6-methyl-2-pyridinecarboxylic acid) (H^3tpaa) containing three picolinate groups with a longitudinal relaxivity value of 13.3 mM^{-1} s^{-1} at 1.4 T and 25 °C, and the stability was observed to be low.[47] In a subsequent study, they synthesized a Gd(III) complex with an octadentate *N*,*N*′-bis[(6-carboxy-2-pyridylmethyl]ethylenediamine–*N*,*N*′-diacetic acid (H_4bpeada) ligand, which has two picolinate groups with a longitudinal relaxivity of 5.0 mM^{-1} s^{-1} at a magnetic field of 20 MHz and 25 °C.[48] This relaxivity value is greater than for DOTA ($r_1 = 4.7$ mM^{-1} s^{-1}) and DTPA ($r_1 = 4.8$ mM^{-1} s^{-1}).[49] The stability of this octadentate ligand (H_4bpeda) is less than that of the ethylenediaminetetraacetic acid (H_4EDTA) ligand, which is hexadentate in nature. Furthermore, the same group synthesized the ligand *N*,*N*′-bis[(6-carboxy-pyridin-2-yl)methyl]glycin (H_3dpaa),[50] replacing one of the picolinate groups with a carboxylate group. The ligand H_3dpaa exhibits a relaxivity value of 11.93 mM^{-1} s^{-1} at 4.7 T and 25 °C, with stability higher than the H_3tpaa ligand. Based on the aforementioned discussions, Phukan *et al.*[51] synthesized a ligand H_4peada with one picolinate and three carboxylate groups to obtain higher relaxivity and stability. Later, they synthesized a hexadentate ligand (H_3cbda) with two picolinate and one carboxylate group to incorporate both the relaxivity and thermodynamic stability with a methyl group in the backbone of the ligand.[52]

On account of the above perspectives, the present computational study uncovers the thermodynamic stability and comparative binding affinities of heptadentate ($peada^{4-}$ and $tpaa^{3-}$) and hexadentate ($cbda^{3-}$ and $dpaa^{3-}$) ligands with Ln^{3+} ions in aqueous solution. Furthermore, the trend in the water exchange rate (k_{ex}) of the inner-sphere water with bulk water has been investigated, following the methodology proposed by Figueroa *et al.*[53] Moreover, this work computationally ascertained the type of mechanism for the coordinated water molecules based on the activation parameter values. The ligands chosen in this study are shown in Scheme 1.[47,50–52] In addition, the bonding interactions between the metal and ligand have been confirmed by the Quantum Theory of Atoms-In-Molecules (QTAIM) and energy decomposition analysis (EDA). This sheds light on the different binding affinity of the ligand with Ln^{3+} ions. Thus we believe that the thermodynamic stability and mechanistic overview of the water exchange rate kinetics provided in this study will be helpful in future ligand designing for stable lanthanide-based complexes. The last segment concludes our analyses.

2 Computational details

All the geometries of the lanthanide complexes were optimized with relativistic DFT, using the hybrid meta-GGA TPSSh functional[53,54] as implemented in the Gaussian 16 program

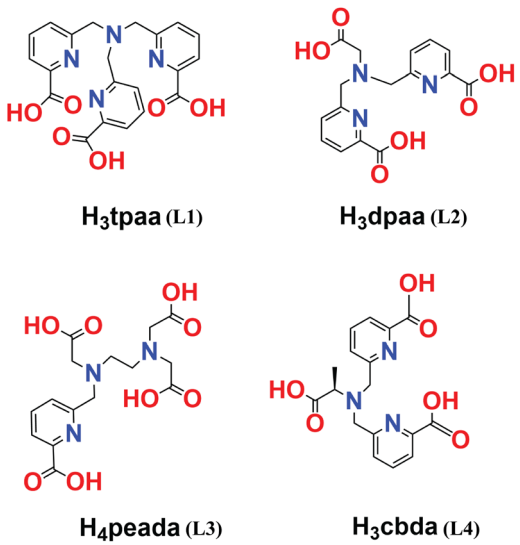

Scheme 1 Ligands (L1 (ref. 47)), (L2 (ref. 50)), (L3 (ref. 51)) and (L4 (ref. 52)) considered in this study.

package.[55] The vibrational frequency analysis has been carried out to characterize the nature of the optimized geometries as energy minima or saddle points. Additionally, we tested the performance of different density functionals (B3LYP, B3LYP-D3, and ωB97XD) for comparative purposes. The choice of the TPSSh functional is due to its better geometrical interpretation than the hybrid GGA (B3LYP) functional.[53,56] Also, the long-range corrected functional (ωB97XD) does not provide a better geometrical interpretation than the hybrid meta-GGA (TPSSh) functional. Hence we used the TPSSh functional during the geometry optimization of the complexes. For the central metal atom (Ln^{3+}), we considered both large core relativistic effective core potential (LCRECP) with its related (7s6p5d)/[5s4p3d]-GTO valence basis set,[57] and small core relativistic effective core potential (SCRECP)[58] with the ECP28MWB_GUESS[53] basis set for comparative purposes. The standard 6-31G(d,p) and 6-31+G(d,p) (for some specific calculations) basis sets were applied for the remaining elements (H, C, N, and O). The performance of different density functionals and basis sets is discussed in detail in the dedicated sections below. At the same level of theory, the transition state geometries were located and the intrinsic reaction coordinate (IRC) paths were generated. Furthermore, to correct the activation energy barrier, we calculated the single point energy (taking the large core DFT optimized geometry) of the reactant and transition state by considering the wave function-based method, second order Møller–Plesset perturbation theory (MP2),[59] with the def2-TZVP basis set for the remaining elements (H, C, N, and O).

The computational investigations of lanthanide complexes using relativistic effective core potential (ECP)[60–62] in conjugation with density functional theory (DFT) provide accurate results for most of the earlier reported complexes.[63,64] It has been mentioned earlier that large-core (LC) calculations provide a somewhat longer bond distance than that of the small-core (SC) calculations.[53] Despite its approximate nature, LCRECP is an efficient computational tool, which focuses mainly on the analysis of geometrical structures and estimation of relative energies of heavy metal-containing complexes at the DFT level.[53,65,66]

Moreover, to incorporate the solvent effect, the polarizable continuum model (PCM)[67,68] with the integral equation formalism, *i.e.* the IEFPCM[67] model, has been considered. To describe the accurate M–L bond and ^{17}O hyperfine coupling constant values, we have explicitly considered the second sphere of water along with the implicit solvent model (IEFPCM).[69,70] To describe the cavity of the solvent, universal force field radii[71] were applied and adjusted by a factor of 1.1. Optimization was carried out by imposing nosymm constraints. Furthermore, to evaluate the Gibbs free energy values, the solvation model based on density (SMD) has been applied to incorporate the non-electrostatic contributions.[72] Harmonic approximation was applied for the Gibbs free energy calculations at $T = 298.15$ K using five different density functionals (B3LYP, TPSSh, M06,[73] B3LYP-D3, and ωB97XD).

Wave function analysis was performed by applying Bader's Quantum Theory of Atoms-In-Molecules (QTAIM)[74] to obtain the electron density (ρ), electron localization function (ELF) and Laplacian of electron density ($\nabla^2\rho$) at the bond critical points (BCPs) using the Multiwfn program (version 3.8).[75] Furthermore, for the extended transition state (ETS) energy decomposition analysis,[76] optimized structures of the $[Ln(cbda)(H_2O)_3]\cdot 6H_2O$ and $[Ln(peada)(H_2O)_2]^-\cdot 4H_2O$ complexes were considered, having been obtained from the scalar relativistic[77] ZORA[78,79] method, along with the SARC-ZORA[80] basis set for the Ln^{3+} ion and the 6-31G(d,p) basis set for the rest of the elements. From these optimized structures, a single point energy decomposition analysis was performed in the ADF2021 package,[81] using SARC-ZORA approximation with the TZ2P[82] basis set for all the elements, and BP86 functional[83–85] with no frozen core approximation. This ETS analysis has been performed for the closed shell La^{3+} and Lu^{3+} metal centres. Due to their closed shell character, spin restricted formalism was applied.

The ORCA 4.0 program[86] package was used for the analysis of isotropic ^{17}O and ^{1}H hyperfine coupling constants, using TPSSh and the SARC2-DKH-QZVP[87] basis set for the Gd^{3+} ion and the DKH-def2-TZVPP[80] basis set for the remaining atoms.

The molecular electrostatic potential (MEP) at any point in space with position vector $\boldsymbol{r}$ and $\boldsymbol{r}'$ for evaluating the charge distribution of the complexes can be evaluated by applying eqn (1)

$$\sum_{A} Z_A \Big/ |R_A - \boldsymbol{r}| - \int \rho(\boldsymbol{r}') \Big/ |\boldsymbol{r}' - \boldsymbol{r}| \mathrm{d}\boldsymbol{r}' = V(\boldsymbol{r}) \quad (1)$$

where the charge of the nucleus A at a distance R_A is denoted by Z_A and the total density of electrons is $\rho(\boldsymbol{r}')$.[88,89] The MEP of the complexes was calculated using the Multiwfn program (version 3.8).[75]

The M–L binding energies (BEs) were evaluated from the optimized structures of the complexes (both LC- and SC-optimized). The BEs were calculated by individually optimizing the geometries of the complexes, ligands (Scheme 1), and inner-sphere water molecules. This includes basis set superposition error (BSSE) corrections using the counterpoise method[90] for the gas phase optimized structures of the complexes. The BEs of the ligands were also evaluated by doing single point energy calculations using the TPSSh functional and LCRECP (for the Gd^{3+} ion) along with the def2-TZVP[91] basis set for the remaining elements (H, C, N, and O) to reduce the BSSE.

3 Results and discussion

3.1 Stability analysis of the Ln^{3+} complexes

The stability of the Ln^{3+} complexes in aqueous solution is an important issue for the application of Ln^{3+} complexes, which can be decided mainly by two factors: (i) the binding energy of the ligand to the metal ions and (ii) the solvation-free energy of the complexes and free metal ions. In the following two sections, these two factors are analyzed in detail.

3.1.1 Comparative binding energy (BE) calculations of the complexes. Initially, to ensure the strength of the ligands shown in Scheme 1 with Gd^{3+} ions, the binding energies of the complexes were investigated. The optimized structures of the

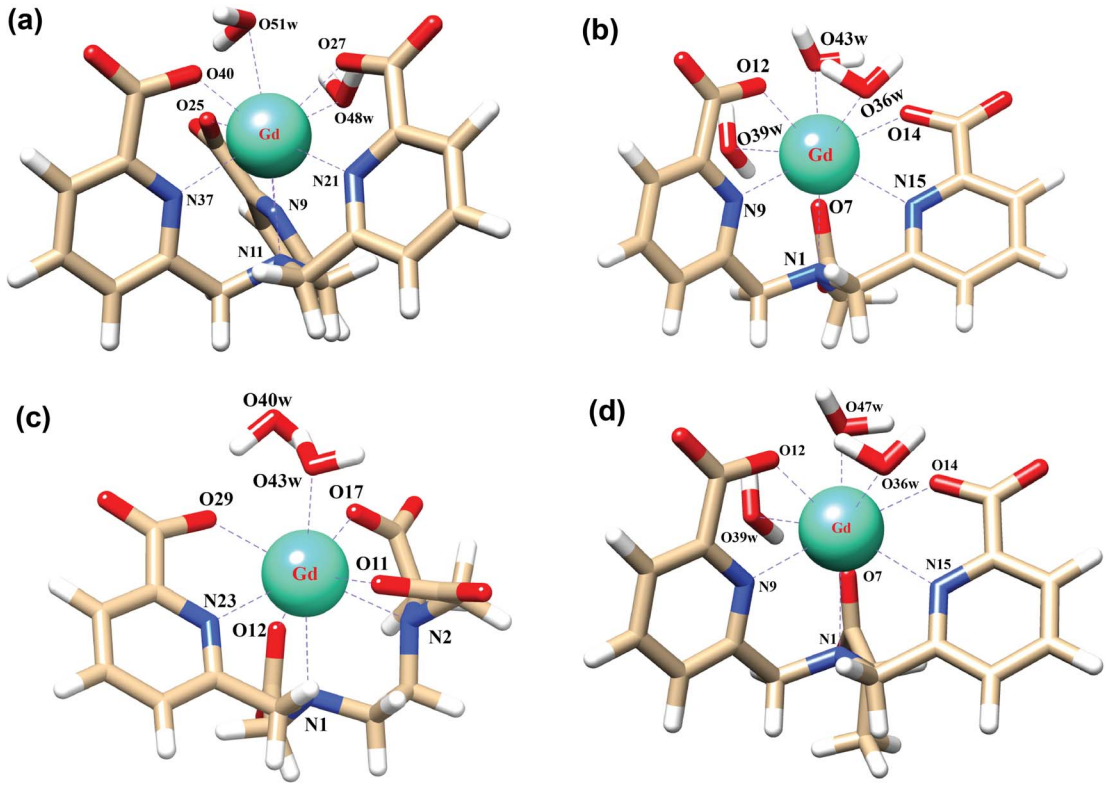

Fig. 1 Optimized structures of (a) $[Gd(tpaa)(H_2O)_2]$, (b) $[Gd(dpaa)(H_2O)_3]$, (c) $[Gd(peada)(H_2O)_2]^-$, and (d) $[Gd(cbda)(H_2O)_3]$ complexes in aqueous solution using the TPSSh/SCRECP/6-31G(d,p) level of theory without considering the second sphere waters.

complexes considered for comparative binding energy calculations are shown in Fig. 1. The results provided herein illustrate that the binding affinity of the ligand $peada^{4-}$ (-197.13 kcal mol^{-1}) with a Gd^{3+} ion is about +31.4 kcal mol^{-1} higher than that of the $tpaa^{3-}$ ligand (-165.73 kcal mol^{-1}) as depicted in Table S1† of the ESI, which agrees with the experimental results.[51]

This is owing to the presence of the three carboxylate groups which bind more strongly to Gd^{3+} due to the oxyphilic nature of the Gd^{3+} ion.[51] Also, the binding affinity of the ligand $cbda^{3-}$ (-166.42 kcal mol^{-1}) is about +1.36 kcal mol^{-1} greater than that of the $dpaa^{3-}$ ligand (-165.06 kcal mol^{-1}). This may be due to the chirality induced by the methyl group in the ligand (H_3cbda) in accordance with the experimental results.[52] Evaluation of BE values using two different core definitions – large core and small core pseudopotentials – (Table S2† in the ESI) regarding both sets of complexes (hexa and heptadentate) provided a similar trend in BE values. In order to justify our method, we further analyzed the BE values of the respective ligands with the Gd^{3+} ion by changing the basis sets (6-31+G(d,p) and def2-TZVP) and methods (B3LYP, B3LYP-D3, and ωB97XD) from the LC optimized structure. The M–L bond distances of all the complexes (Fig. 1) are presented in Tables S3–S6† in the ESI. Lastly, all the data obtained using different density functionals (TPSSh, B3LYP, B3LYP-D3, and ωB97XD) and basis sets (6-31G(d,p), 6-31+G(d,p), and def2-TZVP) along with the different core definitions (LC and SC) are reported in Table S2† of the ESI and provide similar trends towards the relative stability of the complexes.

3.1.2 Estimation of thermodynamic stabilities. To gain further insights into the reasons behind the relative thermodynamic stabilities of the ligands (Scheme 1) with the Gd^{3+} ion, the free energy of formation of the complexes was estimated by using the methodology developed by Figueroa *et al.*[23,92] The thermodynamic cycle to determine the free energy of formation of the ligands $dpaa^{3-}$ and $cbda^{3-}$ with a Gd^{3+} ion is presented in Scheme 2.

As expected,[52] the $\Delta G_{(g)}$ and $\Delta G_{(aq)}$ values tend to be negative on replacing the hexadentate $dpaa^{3-}$ ligand with the $cbda^{3-}$ ligand. The negative $\Delta G_{(g)}$ and $\Delta G_{(aq)}$ indicate the stronger binding affinity of the $cbda^{3-}$ ligand with the Gd^{3+} ion than the $dpaa^{3-}$ ligand, both in the gas phase and solution phase. This again confirms the influence of the methyl group in the ligand

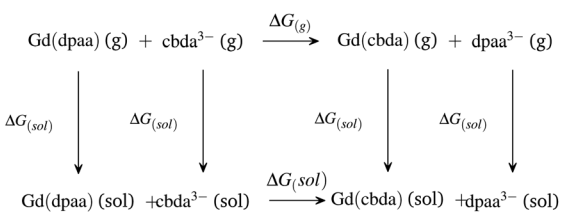

Scheme 2 Thermodynamic cycle for explaining the comparative stabilities of [Gd(cbda)] and [Gd(dpaa)] complexes.

backbone for increased stability of the [Gd(cbda)] complex compared to the [Gd(dpaa)] complex. Different density functionals (B3LYP, TPSSh, M06, B3LYP-D3 and ωB97XD) and core definitions (large core and small core) provide a similar trend in the $\Delta G_{(g)}$ and $\Delta G_{(aq)}$ values and ligand selectivity as shown in Table S7† of the ESI.

Similarly, for the heptadentate ligand bearing $[Gd(peada)]^-$ and [Gd(tpaa)] complexes, the thermodynamic stabilities of the ligands $peada^{4-}$ and $tpaa^{3-}$ with the Gd(III) ion were analyzed (Scheme S1† in the ESI). In this case, it was found that the $[Gd(peada)]^-$ complex formation is more stable than for the [Gd(tpaa)] complex, with higher negative $\Delta G_{(g)}$ and $\Delta G_{(aq)}$ values (Table S7† in the ESI) as a consequence of the presence of four negative carboxylate groups compared to the $tpaa^{3-}$ ligand. These stability trends follow the experimental analysis of the thermodynamic stability of the complexes.[51,52] The experimental $\Delta G^{exp}_{(aq)}$ values, as shown in Tables S7 and S8,† were estimated from the equilibrium constant values provided in the earlier literature.[51,52] Furthermore, different density functionals (B3LYP, TPSSh, M06, B3LYP-D3, and ωB97XD), and basis sets (6-31G(d,p) and 6-31+G(d,p)) impart similar trends in $\Delta G_{(g)}$ and $\Delta G_{(aq)}$ values and ligand selectivity (Tables S7 and S8† in the ESI).

In view of the above stability analysis, we will consider the more stable heptadentate (H_4peada) and hexadentate (H_3cbda) ligands for further investigations.

3.2 Structural analysis

In order to explore the coordination polyhedra and bonding interactions of the ligands ($peada^{4-}$ and $cbda^{3-}$) with lanthanide series elements we have considered the stable La^{3+} ($4f^0$), Gd^{3+} ($4f^7$) and Lu^{3+} ($4f^{14}$) ions. The optimized structures of the $[Ln(peada)(H_2O)_2]^-$ and $[Ln(cbda)(H_2O)_3]$ complexes [Ln = La, Gd, and Lu], obtained using the SC pseudopotential are shown in Fig. 2. The LC-optimized structures are provided in Fig. S1† in the ESI. To limit the drawbacks of the continuum solvation model,[69,93,94] six explicit water molecules for the tris-aquated and four explicit water molecules for the bis-aquated complexes have been considered.

The bond distances calculated using SC and LC pseudopotentials (with different density functionals) are provided in Tables S9–S12† in the ESI. According to previous investigations,[53] the bond length values are longer for LCRECP than SCRECP, which is also reflected in this analysis. The bond length values are in good agreement with the previously synthesized $q > 1$ complex.[43,95] The labilities of the three water molecules in tris-aquated $[Gd(cbda)(H_2O)_3]\cdot 6H_2O$ and the two water molecules in the $[Gd(peada)(H_2O)_2]^-\cdot 4H_2O$ complex were found to be different based on the bond length analysis and the complexes are anticipated to exhibit different water exchange rates (k_{ex}).

The bond length values decrease along the series as predicted as a consequence of the lanthanide contraction, as shown in Fig. 3(a) and (b). The values calculated using SCRECP decreased from La^{3+} to Lu^{3+} with some fluctuation. At first, for the tris-aquated complex the bond length values follow the trend Ln–O36 (w) > Ln–O39 (w) > Ln–O47 (w), and the

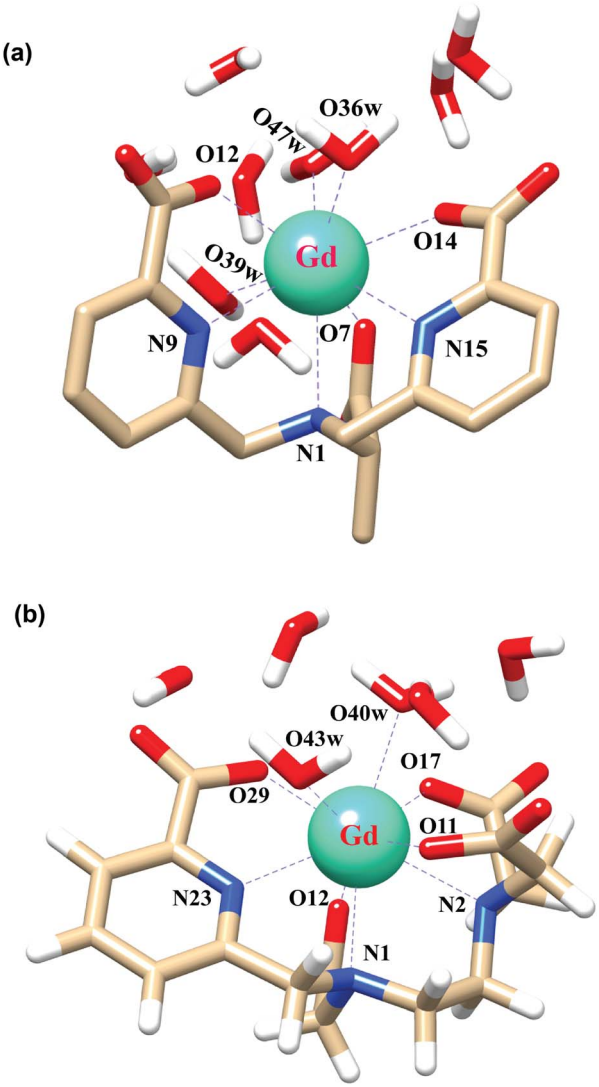

Fig. 2 Optimized structures of the complexes (a) $[Gd(cbda)(H_2O)_3]\cdot 6H_2O$, and (b) $[Gd(peada)(H_2O)_2]^-\cdot 4H_2O$ with second sphere waters obtained using the SCRECP/TPSSh/6-31G(d,p) level of theory.

fluctuations of the bond lengths were higher for Ln–O36 (w) and Ln–O39 (w) compared to Ln–O47 (w) due to the steric and pulling effects of water molecules, which reflects the weaker binding of the water molecules as shown in Fig. 3(a). In the bis-aquated complex, the bond length values follow the trend Ln–O40 (w) > Ln–O43 (w) (Fig. 3(b)).

Moreover, the average Ln–N bond length values for the tris-aquated and bis-aquated complexes decrease from 2.79 to 2.66 Å and 2.77 to 2.57 Å respectively. Whereas, the Ln–O (carboxylate) bond length only drops from 2.49 to 2.33 Å and 2.43 to 2.27 Å respectively (Tables S7–S10† in the ESI). In both bis and tris-aquated metal co-ordination polyhedra, the shortest distance is between the Ln^{3+} ion and the carboxylate oxygen because of the hard–hard interaction of oxygen and the Ln^{3+} ion according to Pearson's HSAB concept.[96]

The metal–(H_2O) bond strength was further confirmed by analysis of the electron density (ρ_{BCP}), the Laplacian of the

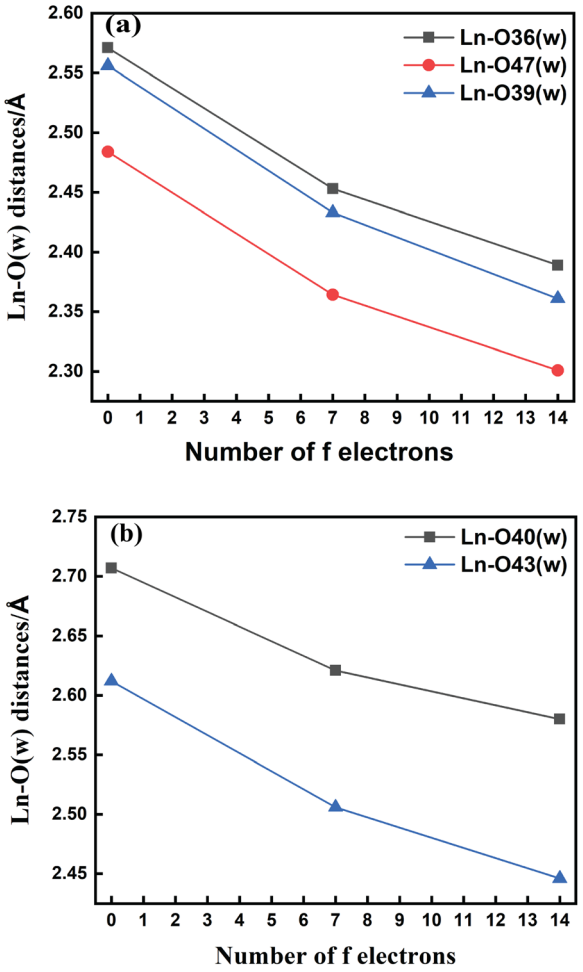

Fig. 3 Variation of Ln–O (w) bond lengths along the lanthanide series for (a) $[Ln(cbda)(H_2O)_3]\cdot 6H_2O$ and (b) $[Ln(peada)(H_2O)_2]^-\cdot 4H_2O$ complexes obtained using the SCRECP/TPSSh/6-31G(d,p) level of theory (Ln = La, Gd and Lu).

electron density ($\nabla^2\rho$), and the electron localization function (ELF) at the critical points of the respective bonds along the Ln^{3+} (Ln = La, Gd, and Lu) series as presented in Tables S11–S14† in the ESI. Our investigations show that for the tris-aquated complex the ρ_{BCP} values follow the trend Ln–O47 (w) > Ln–O39 (w) > Ln–O36 (w) as shown in Fig. 4(a). Similarly, for the bis-aquated complex the ρ_{BCP} value follows the trend Ln–O43 (w) > Ln–O40 (w) (Fig. 4(b)), opposite to that of bond length values. These ρ_{BCP} values tend to increase in the series' first half and then decrease. The decrease of the electron density indicates weaker binding of the inner-sphere water molecules.[53,97] Again, the ELF values decrease along the lanthanide series as ionic radii decrease. However, the bond length becomes shorter, indicating the weaker binding of water molecules at the end of the series as shown in Fig. 4(c) and (d). This agrees well with the labile capping bond phenomenon mentioned in previous literature.[97]

The Ln–O (w) bond length values of the anionic $[Ln(peada)(H_2O)_2]^-\cdot 4H_2O$ complex are longer than those of the neutral $[Ln(cbda)(H_2O)_3]\cdot 6H_2O$ complex, which indicates the faster k_{ex} in the anionic complex.[45] Furthermore, the calculation of the electron density (ρ_{BCP}), ELF, and Laplacian of the electron density ($\nabla^2\rho$) using the LC pseudopotential ensures the reliability of the SC pseudopotential for electron density calculations for $q > 1$ complexes.

3.3 Evaluation of water exchange kinetics

3.3.1 Stable hydration number (q) calculations for both bis-aquated and tris-aquated complexes. The determination of the hydration state of Gd(III) complexes in aqueous solution is a challenging task.[98] Yet, to understand the water exchange kinetics and relaxivity of Gd(III) complexes, understanding the hydration state of Gd(III) complexes is crucial. The relaxivity of Gd(III) complexes increases with an increase in q.[31] Therefore, before determining the water exchange rate, we first analysed the stable hydration number of the complexes. We explore the stable hydration number of the tris-aquated $[Gd(cbda)(H_2O)_3]\cdot 6H_2O$ and bis-aquated $[Gd(peada)(H_2O)_2]^-\cdot 4H_2O$ complexes using three different density functionals (B3LYP, TPSSh, and M06-2X[73]). To calculate the stable hydration number of the complexes, we have explored a relaxed potential energy surface scan of the complexes, by changing the bond length values of each of the inner-sphere water molecules from the equilibrium conformation, using a step size of 0.05 Å as shown in Fig. 5. These relaxed scans show that the nine coordinated $[Gd(cbda)(H_2O)_3]\cdot 6H_2O$ is more stable than the eight coordinated $[Gd(cbda)(H_2O)_2]\cdot 7H_2O$ complex as shown in Fig. 5(a)–(c). This is in accordance with the available experimental findings.[52] All three density functionals (B3LYP, TPSSh, and M06-2X)[98] provide similar trends in stable hydration number.

Based upon the above analysis, for the bis-aquated $[Gd(peada)(H_2O)_2]^-\cdot 4H_2O$ complex we considered only one functional (TPSSh). An intensive assessment of other functionals was not carried out for the bis-aquated complex. In the case of the bis-aquated complex, scanning of the Gd–O40 (w) bond stabilized the eight coordinated $[Gd(peada)(H_2O)]^-\cdot 5H_2O$ and the scanning of Gd–O43 (w) stabilized the nine coordinated $[Gd(peada)(H_2O)_2]^-\cdot 4H_2O$ complex, in accordance with the experimental analysis[51] of the hydration equilibria, showing the co-existence of both eight and nine coordinated forms as shown in Fig. 5(d) and (e). This co-existence is due to the flexible ligand environment due to the presence of four carboxylate groups. The relaxed PES scans for both complexes obtained using the SC pseudopotential are provided in Fig. S2† in the ESI.

3.3.2 Hyperfine coupling constants (HFCCs) of the inner-sphere water molecules. Computational investigations of the hyperfine interaction (HFI) of the coordinated water molecules with the metal centre (Gd^{3+}) have been carried out to deliver a brief illustration of the water exchange rate. During the last few decades, enormous improvements have been made in the study of HFI. Among them, DFT can be extensively used for systems containing a large number of atoms with experimental accuracy.[69,93,94] The ^{17}O and ^{1}H HFCC values are very sensitive to the change in bond length and the direction and position of the inner-sphere water molecule plane with the Gd–O vector.[69] Therefore, applying the methodology proposed by Esteban-

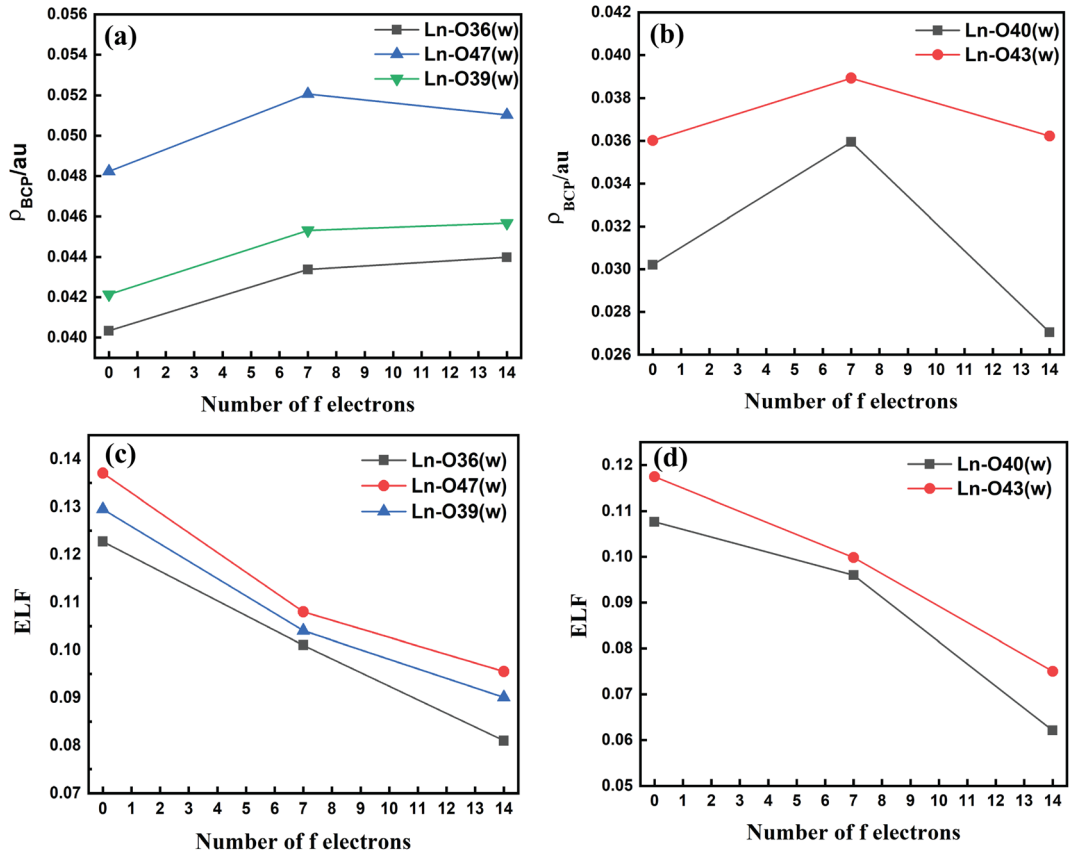

Fig. 4 Electron density (ρ_{BCP}) and electron localization function (ELF) values along the lanthanide series for both $[Ln(Lcbda)(H_2O)_3]\cdot 6H_2O$ (a and c) and $[Ln(peada)(H_2O)_2]^-\cdot 4H_2O$ (b and d) complexes obtained using the SCRECP/TPSSh/6-31G(d,p) level of theory (Ln = La, Gd, and Lu).

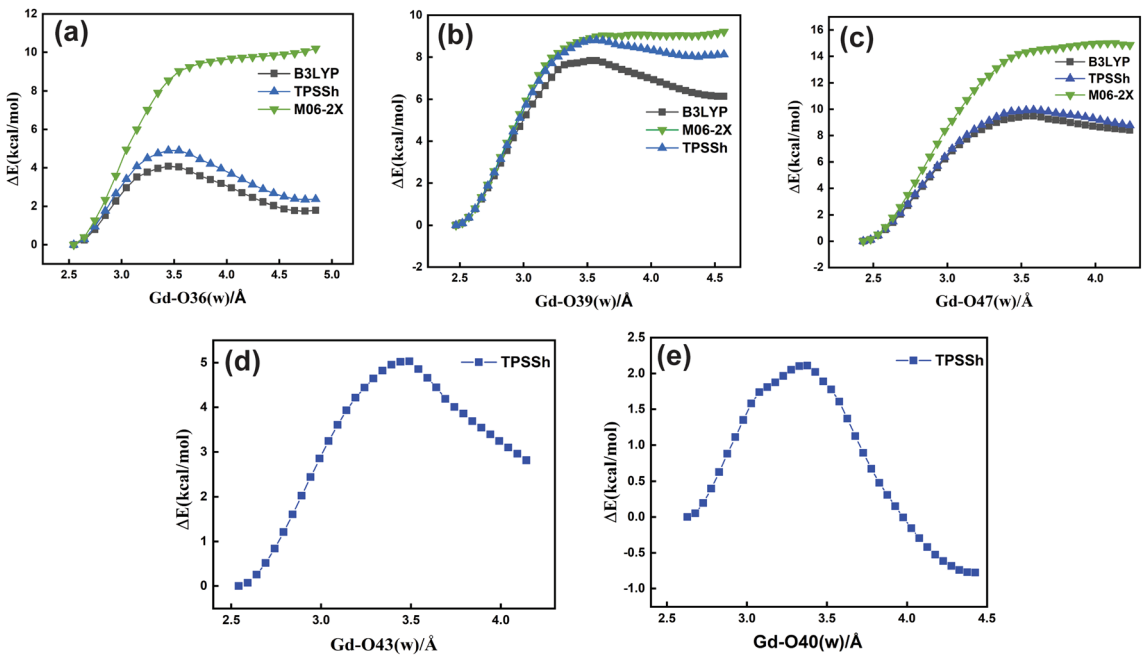

Fig. 5 Relaxed potential energy surface scans for the $[Gd(cbda)(H_2O)_3]\cdot 6H_2O$ complex (top) (a–c) and $[Gd(peada)(H_2O)_2]^-\cdot 4H_2O$ (bottom) (d and e) using LCRECP for Gd^{3+} and the 6-31G(d,p) basis set for other elements with different density functionals.

Gómez *et al.*,[69] we have calculated the HFCCs of the coordinated water molecules in both complexes as presented in Table 1. The three water molecules in the $[Gd(cbda)(H_2O)_3]\cdot 6H_2O$ complex have different HFCC values in accordance with the different Gd–O (w) bond lengths. Similarly, in the bis-aquated $[Gd(peada)(H_2O)_2]^-\cdot 4H_2O$ complex, the two water molecules have significantly different ^{17}O HFCC values, with one having an extremely low value (0.2156 MHz) due to the existence of hydration equilibria for this complex.[51] Moreover, the isotropic (A_{iso}) HFCC values for the ^1H nucleus are minimal for these complexes.[99,100]

3.3.3 Water exchange rate (k_{ex}) for the bis-aquated and tris-aquated complexes. To analyze the trend in the k_{ex} of all the coordinated water molecules with the bulk, we considered the Gd–O (w) bond length values. A longer Gd–O (w) bond means a shorter residence time related to the coordinated water molecule as confirmed by the *ab initio* molecular dynamics study of [Gd(HP-DO3A)].[101] With an increase in the bond length, the residence time of the water molecule decreases.[36,53] Thus, a longer bond length value implies a faster k_{ex} value following a dissociative type of mechanism. Therefore, we will apply the model proposed by Figueroa *et al.*[53] to elucidate the k_{ex} by calculating ρ_{BCP} and ELF at the bond critical point of the respective bond. As a result, the three water molecules in $[Gd(cbda)(H_2O)_3]\cdot 6H_2O$ and two water molecules in $[Gd(peada)(H_2O)_2]^-\cdot 4H_2O$ have significantly different k_{ex} values. The results are presented in Table 2. We employ eqn (2) and (3) for LCRECP, and eqn (4) and (5) for SCRECP to evaluate k_{ex} values computationally.[53] The k_{ex} values obtained using LC optimized geometries with different density functionals (TPSSh, B3LYP, B3LYP-D3, and ωB97XD) are listed in Tables S15 and S16† in the ESI. The k_{ex} follows a similar trend for all the density functionals (except B3LYP).[56,102]

For LCRECP,

$$\rho_{BCP} = 0.05941 - 0.00316 \log k_{ex} \quad (2)$$

$$ELF = 0.13532 - 0.00503 \log k_{ex} \quad (3)$$

For SCRECP,

$$\rho_{BCP} = 0.06440 - 0.00325 \log k_{ex} \quad (4)$$

$$ELF = 0.12275 - 0.00296 \log k_{ex} \quad (5)$$

From this analysis, we can conclude that the water exchange rate in bis and tris-aquated complexes is mainly related to the strength of the Gd–O (w) bond to reach the eight coordinated transition state (TS). The relatively high water exchange rate of the $[Gd(peada)(H_2O)_2]^-\cdot 4H_2O$ complex is due to the overall negative charge of the complex, as anionic complexes exhibit a faster k_{ex} than neutral complexes.[45] Among the two water molecules, Gd–O40 (w) with a bond length of 2.62 Å shows a very high k_{ex}, which may be related to the hydration equilibrium between the mono and bis-aquated forms and the flexible coordination sphere surrounding the Gd^{3+} ion.

3.3.4 Mechanism of water exchange. DFT-based methods have been applied widely for the investigation of the water exchange rate and mechanism of metal-containing complexes.[103] To elucidate whether factors other than the bond strength can also affect the k_{ex}, a mechanistic study of the water exchange rate has been conducted and the corresponding activation parameter values of the complexes were calculated (Table 3). Generally, water exchange of the inner-sphere water molecules with bulk water for nine coordinated complexes mostly follows a dissociative mechanism.[104] To locate the TS, we optimized the structure that connects the nine and eight-coordinated forms of the complexes. The optimized TSs of the complexes are shown in Fig. S3 and S4† in the ESI. An elongated Gd–O (w) bond facilitates faster exchange for a dissociative type of mechanism.[53] Thus, the Gd–O (w) bond length values at the transition states (TSs) indicate a dissociative mechanism, where a water molecule in the inner-sphere leaves the metal coordination environment. The Gd–O (w) bond length values of both tris-aquated $[Gd(cbda)(H_2O)_3]\cdot 6H_2O$ and bis-aquated $[Gd(peada)(H_2O)_2]^-\cdot 4H_2O$ complexes increase in the transition state (TS) compared with their elementary states as shown in Table 3. In the case of the tris-aquated complex, the values increase from 2.53 Å, 2.46 Å and 2.42 Å to 3.48 Å, 3.37 Å, and 3.55 Å, for Gd–O36 (w), Gd–O39 (w) and Gd–O47 (w), respectively. Similar results are obtained in the case of the bis-aquated complex (Table 3). Thus, this confirms that a water molecule in the inner coordination sphere leaves the metal coordination environment, following a dissociative mechanism.

Moreover, we observe that the activation free energy ($\Delta G^{\ddagger}$) values increase with a decrease in the bond length for both complexes (Table 3). The analysis of the activation enthalpies ($\Delta H^{\ddagger}$) provides a shred of additional evidence for faster water

Table 1 ^{17}O and ^1H hyperfine coupling constant values calculated for $[Gd(cbda)(H_2O)_3]\cdot 6H_2O$ and $[Gd(peada)(H_2O)_2]^-\cdot 4H_2O$ complexes using the TPSSh/DKH2/SARC2-DKH-QZVP (Gd)/DKH-def2-TZVPP (other atoms)/SMD method

Ligand	Gd–O (w) (Å)	$^{17}O(A_{iso})$ (MHz)	^1H (MHz)
$cbda^{3-}$	Gd–O36 (w) = 2.45	0.5491	0.0227/0.0390
	Gd–O39 (w) = 2.43	0.6052	0.0633/0.0696
	Gd–O47 (w) = 2.36	0.9661	0.0220/0.0350
$peada^{4-}$	Gd–O40 (w) = 2.62	0.2156	0.0536/0.0517
	Gd–O43 (w) = 2.50	0.4724	0.0746/0.0102

Table 2 Calculated Gd–O (w) bond length, (ρ, au), ELF, and k_{ex}^{298} values of $[Gd(cbda)(H_2O)_3]\cdot 6H_2O$ and $[Gd(peada)(H_2O)_2]^-\cdot 4H_2O$ complexes obtained using the SCRECP/TPSSh/6-31G(d,p) method

Ln–O (w)bond length	ρ_{BCP}	ELF	$k_{ex}^{298}/10^6$ s^{-1}
$[Gd(cbda)(H_2O)_3]\cdot 6H_2O$			
Gd–O36 (w) = 2.453	0.04338	0.101	22.16
Gd–O39 (w) = 2.433	0.04532	0.104	1.4
Gd–O47 (w) = 2.364	0.05207	0.108	0.10
$[Gd(peada)(H_2O)_2]^-\cdot 4H_2O$			
Gd–O40 (w) = 2.621	0.0359	0.0959	750.5
Gd–O43 (w) = 2.506	0.03893	0.0998	56.6

Table 3 Activation parameter values for $[Gd(cbda)(H_2O)_3]\cdot 6H_2O$ and $[Gd(peada)(H_2O)_2]^-\cdot 4H_2O$ complexes obtained using LCRECP/TPSSh/6-31G(d,p) and activation energy values calculated using the MP2/LCRECP/def2-TZVP level of theory

		$[Gd(cbda)(H_2O)_3]\cdot 6H_2O$			$[Gd(peada)(H_2O)_2]^-\cdot 4H_2O$	
Methods		Gd–O36 (w)	Gd–O39 (w)	Gd–O47 (w)	Gd–O40 (w)	Gd–O43 (w)
TPSSh	$\Delta E_a^{\ddagger}$ (kcal mol^{-1})	4.93	8.90	9.95	2.10	5.02
	r_{Gd-O}/Å	2.53	2.46	2.42	2.63	2.54
	$r_{Gd-O(TS)}$/Å	3.48	3.37	3.55	3.35	3.45
	$\Delta H^{\ddagger}$ (kcal mol^{-1})	4.26	8.31	9.25	1.34	4.32
	$\Delta G^{\ddagger}$ (kcal mol^{-1})	3.95	7.70	8.40	1.25	3.57
	$\Delta S^{\ddagger}$ (J mol^{-1} K^{-1})	4.35	9.20	11.84	1.37	10.46
MP2	$\Delta E_a^{\ddagger}$ (kcal mol^{-1})	4.24	8.67	8.80	1.43	4.54

exchange in Gd–O36 (w) followed by Gd–O39 (w) and Gd–O47 (w) in the tris-aquated complex (Table 3). Further, for the bis-aquated complex, the $\Delta H^{\ddagger}$ value increases drastically from Gd–O40 (w) to Gd–O43 (w). In addition, the positive activation entropies ($\Delta S^{\ddagger}$) (Table 3) indicate a dissociative type of mechanism.[36,105,106] Further, to confirm the nature of the mechanism, we have performed intrinsic reaction coordinate (IRC) calculations (Fig. S5† in the ESI), ensuring the dissociative nature of the mechanism.

We tested both large core (4f, in core) and small core pseudopotentials and found that activation parameter values are sensitive to the choice of the core definitions. But both SCRECP and LCRECP provide a similar trend in the activation parameter values except in Gd–O40 (w) (Table S16† in the ESI). The unexpectedly high water exchange rate (k_{ex}) in Gd–O40 (w) is due to the very low $\Delta H^{\ddagger}$ value, corresponding to the weaker metal and water molecule interaction. Moreover, we have performed single point energy calculations using the MP2 method for a comparative purpose. The DFT (TPSSh) and MP2 methods exhibit quite similar values of activation energies (Table 3).

3.4 Bonding nature of the complexes

3.4.1 Quantum theory of atoms-in-molecules (QTAIM) analysis. The different forms of chemical bond in a compound indicate different chemical and physical properties. Theoretically, the bonding nature between the Ln^{3+} ion and the ligand was characterized with the help of Bader's Quantum Theory of Atoms-In-Molecules (QTAIM) and electron localization function (ELF) analysis. The primary application of QTAIM is the topological analysis of the electron density to characterize the important bonding nature of the M–L bonds. The locations of the respective BCPs in the $[Gd(cbda)(H_2O)_3]\cdot 6H_2O$ and $[Gd(peada)(H_2O)_2]\cdot 4H_2O$ complexes are presented in Fig. 6(a) and (b) respectively. The orange dots indicate the BCPs in M–O/N bonds. The value of ρ_{BCP} and its Laplacian ($\nabla^2\rho$) at the BCPs suggest the type of bonding. The value $\rho_{BCP} < 0.10$ au and the positive Laplacian value signify ionic bonding (Tables S11 and S12† in the ESI). Thus, the electrostatic nature of the bonding is reflected.

Moreover, to assess the bonding interaction between the metal and the ligand a useful quantum mechanical method, *i.e.*

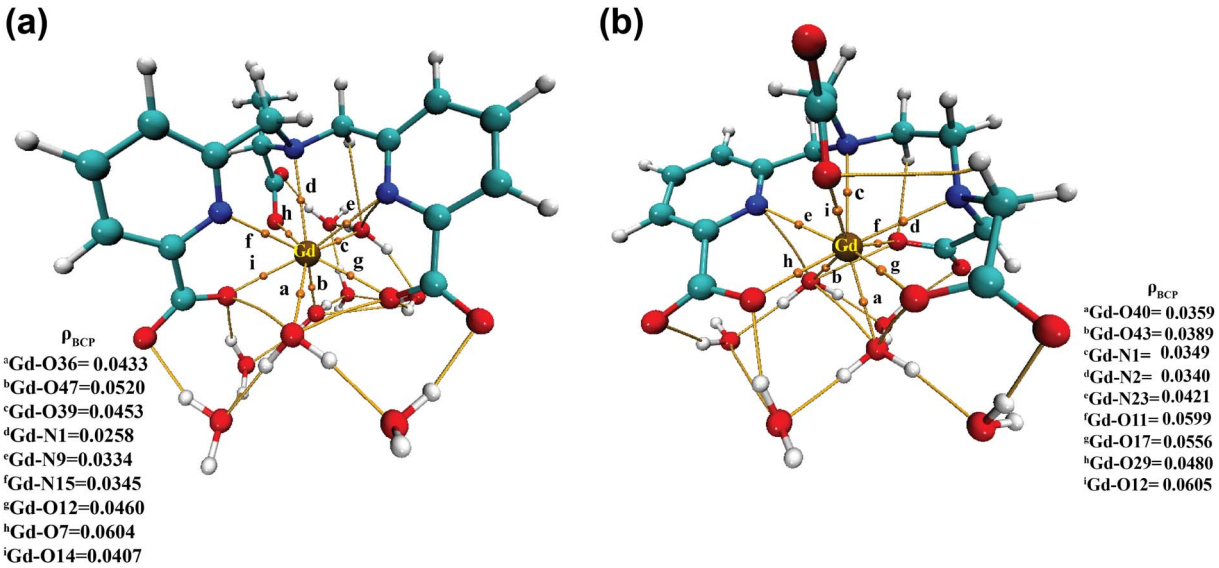

Fig. 6 Electron density (ρ) values at the bond critical points (BCPs) of (a) $[Gd(cbda)(H_2O)_3]\cdot 6H_2O$ and (b) $[Gd(peada)(H_2O)_2]^-\cdot 4H_2O$ complexes.

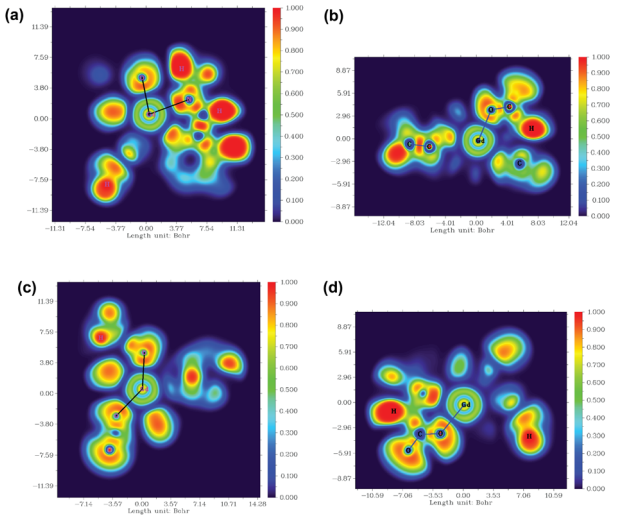

Fig. 7 (a) and (b) ELF plots in the *XZ* and *YZ* planes for the $[Gd(cbda)(H_2O)_3]\cdot 6H_2O$ complex, and (c) and (d) ELF plots in the *XZ* and *YZ* planes for the $[Gd(peada)(H_2O)_2]^-\cdot 4H_2O$ complex.

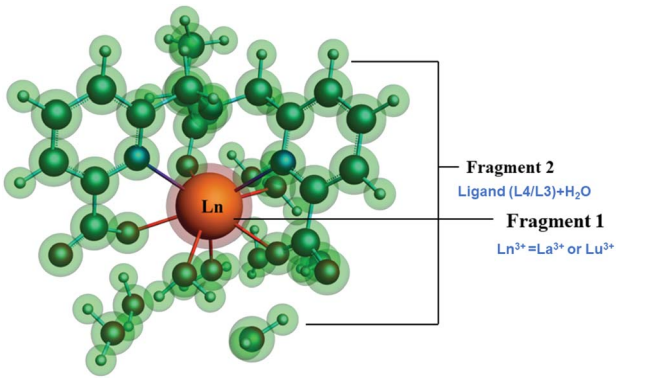

Fig. 8 Schematic representation of different fragmentation modes of the $[Ln(cbda)(H_2O)_3]\cdot 6H_2O$ and $[Ln(peada)(H_2O)_2]^-\cdot 4H_2O$ complexes (Ln = La^{3+} and Lu^{3+}).

the electron localization function (ELF), was employed. ELF is a simple and useful descriptor of the topological analysis of chemical bonds based on Pauli's repulsion effect. Here, the implementation of ELF based on Pauli's repulsion was investigated. In the ELF color-filled map surface (Fig. 7) the region between the metal (Gd^{3+}) and the oxygen or nitrogen atoms of the ligands is considered. The color scale is from 0 (blue) to 1 (red) as shown in Fig. 7. According to Becke and Edgecombe,[107] an ELF value close to 1 (colored red in Fig. 7) indicates the highest Pauli's repulsion zone. While a value close to 0 indicates the minimum Pauli's repulsion zone which is colored blue in the ELF color-filled map (Fig. 7). The highest Pauli's repulsion zone corresponds to the localization of electrons, indicating covalent bonding, but electrons are delocalized in the lowest Pauli's repulsion area. Subsequently in our analysis the ELF values are close to 0 (Tables S11–S14† in the ESI), exhibiting clearly the ionic nature of the M–L bond. Therefore, both atoms-in-molecules (AIM) and ELF results indicate the presence of ionic bonding.

3.4.2 Energy decomposition analysis (EDA). An in-depth analysis of the interaction between the metal and the ligand was further carried out by the extended transition state method (ETS). For this, we have conducted an EDA analysis by considering the closed-shell La^{3+} and Lu^{3+} complexes of hexadentate ($cbda^{3-}$) and heptadentate ($peada^{4-}$) ligands. The different fragmentation modes are shown in Fig. 8. The total interaction energy (ΔE_{int}) between the considered fragments [fragment 1 = Ln^{3+} and fragment 2 = ligand + H_2O] can be represented by the Morokuma–Ziegler energy partitioning model[76] as:

$$\Delta E_{int} = \Delta V_{elst} + \Delta E_{Pauli} + \Delta E_{oi} \quad (6)$$

where ΔV_{elst} represents the classical electrostatic interactions between the different fragments when they are brought together forming the complex, ΔE_{Pauli} is the Pauli repulsion, especially the repulsion due to steric interactions, and ΔE_{oi} represents the orbital interactions.

The detailed physical significance of the above terms has been described by Bickelhaupt and Baerends.[108] The data for the EDA analysis are presented in Table S18† in the ESI. We observed (Table S18†) that the attractive interaction within the M–L complex is derived from the ΔE_{oi} and ΔE_{elst} terms. Moreover, in ionic bonding, ΔE_{oi} is less than ΔE_{elst} but the opposite is true for covalent bonds. In this study, the interaction of the ligand ($cbda^{3-}$ and $peada^{4-}$) with lanthanides (La^{3+}, Lu^{3+}) was evaluated to figure out the strength and the changes in the M–L bonding in the series. In particular, the data presented in Table S18† reflects the following salient features:

(I) A relationship can be derived between the metal complex stability in terms of interaction energy (ΔE_{int}) and the f-electrons. As depicted in Table S18† in the ESI, the ΔE_{int} value of the Lu–ligand (a fully occupied f-shell) complex is higher than that of the La–ligand complex (an empty f-shell).

(II) The electrostatic contribution is about two to three times larger in magnitude than the covalent contribution in f^0 and f^{14} systems, implying that M–L bonding is electrostatic in nature rather than covalent.

(III) Again, as the charge character of the ligand increases from $cbda^{3-}$ to $peada^{4-}$, the electrostatic contribution of the $[Ln(peada)]^-$ complex is larger compared to the [Ln(cbda)] complex. The percentage of electrostatic contribution in the $[Ln(peada)]^-$ complex is also greater than that in the [Ln(cbda)] complex.

(IV) The percentage of electrostatic contribution decreases from La (f^0) to the Lu (f^{14}) system, *i.e.*, the covalent contribution is somewhat larger in the Lu (f^{14}) system.

(V) The Pauli (ΔE_{Pauli}) and orbital ΔE_{oi} contributions do not change markedly upon changing the ligand charges, as they fluctuate only within a few hundred kilojoules per mole.

3.5 Analysis of molecular electrostatic potential (MEP)

Molecular electrostatic potential analysis has been carried out to understand the charge distribution within the respective molecules based on their ligand's denticity (hexadentate or

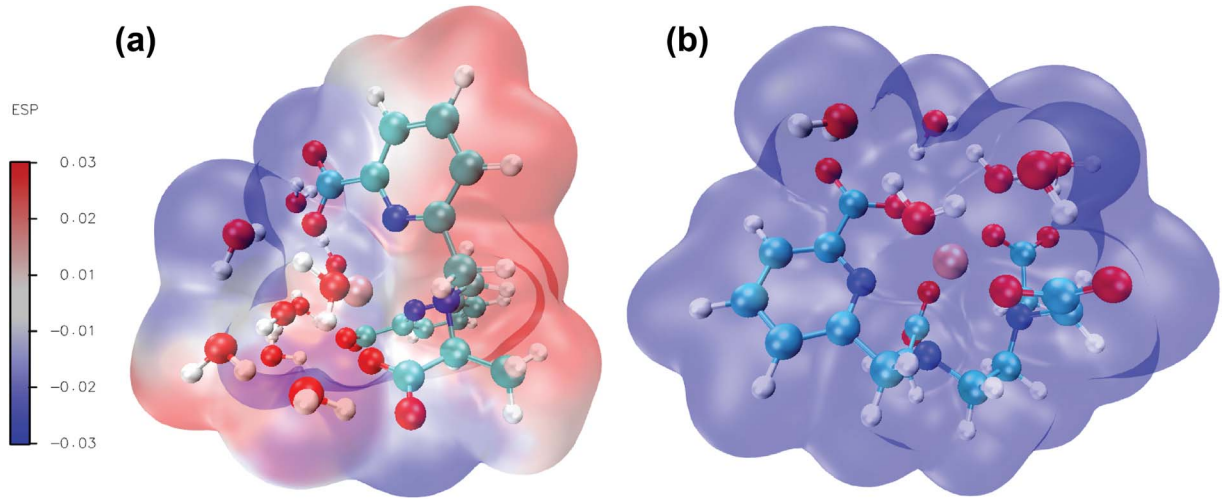

Fig. 9 Computed molecular electrostatic potentials for: (a) $[Gd(cbda)(H_2O)_3]\cdot 6H_2O$ and (b) $[Gd(peada)(H_2O)_2]^-\cdot 4H_2O$ complexes at the SCRECP/TPSSh/6-31G(d,p) theoretical level. The colour bar displays the electron density distribution. Blue represents the highest electron density sites.

heptadentate). This helps evaluate the different interactive behaviour, reactivity and structure of the molecules.[109] As noted earlier,[92] different colors of the molecular surface indicate different interactive areas. On account of this, we have investigated the MEP of the $[Gd(cbda)(H_2O)_3]$ and $[Gd(peada)(H_2O)_2]^-$ complexes as shown in Fig. 9(a) and (b). The molecular surface of the complexes is divided into two regions: hydrophilic (blue) and hydrophobic (red). The blue color of the $[Gd(peada)(H_2O)_2]^-$ complex indicates a hydrophilic area and a more negative electrostatic potential. This is due to a large number of carboxylic groups (four) pointing in the same direction and the overall negative charge of the anionic complex compared to the neutral complex.

In the neutral $[Gd(cbda)(H_2O)_3]$ complex, carboxylate groups (three) are present and attached at different sides of the complex.

4 Conclusions

In summary, the stability of lanthanide complexes fluctuates with the nature of the ligand, and its environment. First, a comparison of the coordination properties and the thermodynamic stability of hexadentate ($cbda^{3-}$ and $dpaa^{3-}$) and heptadentate ($peada^{4-}$ and $tpaa^{3-}$) ligands with the Gd^{3+} ion was carried out in aqueous solution. This stability analysis allows rationalizing that the hexadentate $cbda^{3-}$ ligand forms a reasonably stable complex with the Gd^{3+} ion compared to the $dpaa^{3-}$ ligand. The presence of a methyl group in the ligand backbone causes a slight increase in the selectivity of this ligand. Likewise, the presence of a large number of carboxylate groups in the $peada^{4-}$ ligand causes an increased selectivity of this ligand compared with $tpaa^{3-}$ towards the Gd^{3+} ion. A detailed structural analysis has been carried out for the more stable bis-aquated $[Gd(peada)(H_2O)_2]^-\cdot 4H_2O$ and tris-aquated $[Gd(cbda)(H_2O)_3]\cdot 6H_2O$ complexes at the molecular level. The work also established that the complex $[Gd(cbda)(H_2O)_3]\cdot 6H_2O$ possesses a stable hydration state of three. In contrast, for the $[Gd(peada)(H_2O)_2]^-\cdot 4H_2O$ complex, a hydration equilibrium exists between the mono and bis-aquated forms.

The kinetic study interpretation by analyzing the water exchange rate of the inner-sphere water molecules reveals that water molecules exhibit different k_{ex} rates depending on the ligand environment. The increased water exchange rate is related to the weaker Ln–O(w) bond length, low electron density, and low ELF value. Moreover, from the mechanistic perspective, the dissociative nature of the water exchange mechanism was observed for the exchange of coordinated water molecules with bulk water. However, we have established that for the bis-aquated complex, one coordinated water exhibits an unexpectedly fast k_{ex} rate ($k_{ex}^{298} = 750 \times 10^6\ s^{-1}$). This is due to the existence of hydration equilibria and a flexible ligand environment.

Additionally, this study confirms that the M–L bonding interaction is purely ionic. The percentage of electrostatic contribution increases with the increased charge of the ligand and decreases from La (f^0) to Lu (f^{14}) systems. The interaction energy between the metal and ligand was found to increase in the order $[La(cbda)(H_2O)_3] < [Lu(cbda)(H_2O)_3] < [La(peada)(H_2O)_2]^- < [Lu(peada)(H_2O)_2]^-$. Thus we believe that these findings will be helpful for designing lanthanide-based complexes with higher hydration number and stability. This lights the way for less toxic MRI contrast agents with higher relaxivity.

Conflicts of interest

There are no conflicts to declare.

Acknowledgements

The authors thank the PARAM-ISHAN super-computing facilities for providing high performance computations and the Department of Chemistry, IIT Guwahati for infrastructure

facilities. NK acknowledges the Council of Scientific and Industrial Research (CSIR), India for the fellowship and the financial support, through the registration number 09/731(0167)/2019-EMR-I.

Notes and references

1 D. Parker and J. G. Williams, *J. Chem. Soc., Dalton Trans.*, 1996, 3613–3628.
2 D. Parker, R. S. Dickins, H. Puschmann, C. Crossland and J. A. Howard, *Chem. Rev.*, 2002, **102**, 1977–2010.
3 T. Cheisson and E. J. Schelter, *Science*, 2019, **363**, 489–493.
4 E. Aluicio-Sarduy, N. A. Thiele, K. E. Martin, B. A. Vaughn, J. Devaraj, A. P. Olson, T. E. Barnhart, J. J. Wilson, E. Boros and J. W. Engle, *Chem. - Eur. J.*, 2020, **26**, 1238–1242.
5 N. M. Shavaleev, S. V. Eliseeva, R. Scopelliti and J.-C. G. Bünzli, *Chem. - Eur. J.*, 2009, **15**, 10790–10802.
6 G. R. Motson, J. S. Fleming and S. Brooker, *Adv. Inorg. Chem.*, 2004, **55**, 361–432.
7 J.-C. G. Bunzli, *Chem. Rev.*, 2010, **110**, 2729–2755.
8 A. M. Nonat and L. J. Charbonnière, *Coord. Chem. Rev.*, 2020, **409**, 213192–213207.
9 D. Carpanese, G. Ferro-Flores, B. Ocampo-Garcia, C. Santos-Cuevas, N. Salvarese, M. Figini, G. Fracasso, L. De Nardo, C. Bolzati, A. Rosato, et al., *Sci. Rep.*, 2020, **10**, 1–10.
10 Y.-D. Xiao, R. Paudel, J. Liu, C. Ma, Z.-S. Zhang and S.-K. Zhou, *Int. J. Mol. Med.*, 2016, **38**, 1319–1326.
11 A. Webb, *Anal. Chem.*, 2012, **84**, 9–16.
12 R. D. Alvares, D. A. Szulc and H.-L. M. Cheng, *Sci. Rep.*, 2017, **7**, 1–9.
13 P. Caravan, *Chem. Soc. Rev.*, 2006, **35**, 512–523.
14 P. Marzola, F. Osculati and A. Sbarbati, *Eur. J. Radiol.*, 2003, **48**, 165–170.
15 P. Caravan, C. T. Farrar, L. Frullano and R. Uppal, *Contrast Media Mol. Imaging*, 2009, **4**, 89–100.
16 D. Pan, A. H. Schmieder, S. A. Wickline and G. M. Lanza, *Tetrahedron*, 2011, **67**, 8431–8444.
17 S. Aime, M. Botta, M. Fasano and E. Terreno, *Chem. Soc. Rev.*, 1998, **27**, 19–29.
18 J. Wahsner, E. M. Gale, A. Rodríguez-Rodríguez and P. Caravan, *Chem. Rev.*, 2019, **119**, 957–1057.
19 S. A. Woolen, P. R. Shankar, J. J. Gagnier, M. P. MacEachern, L. Singer and M. S. Davenport, *JAMA Intern. Med.*, 2020, **180**, 223–230.
20 D. Levine, R. J. McDonald and H. Y. Kressel, *JAMA, J. Am. Med. Assoc.*, 2018, **320**, 1853–1854.
21 J. S. McDonald and R. J. McDonald, *Magn. Reson. Imaging Clin. N. Am.*, 2020, **28**, 497–507.
22 M. Port, J.-M. Idée, C. Medina, C. Robic, M. Sabatou and C. Corot, *BioMetals*, 2008, **21**, 469–490.
23 A. Rodriguez-Rodriguez, M. Regueiro-Figueroa, D. Esteban-Gomez, R. Tripier, G. Tircso, F. K. Kalman, A. C. Benyei, I. Toth, A. d. Blas, T. Rodriguez-Blas, et al., *Inorg. Chem.*, 2016, **55**, 2227–2239.
24 B. Zhang, L. Cheng, B. Duan, W. Tang, Y. Yuan, Y. Ding and A. Hu, *Dalton Trans.*, 2019, **48**, 1693–1699.
25 H. U. Rashid, M. A. U. Martines, J. Jorge, P. M. de Moraes, M. N. Umar, K. Khan and H. U. Rehman, *Bioorg. Med. Chem.*, 2016, **24**, 5663–5684.
26 P. D. Garimella, A. Datta, D. W. Romanini, K. N. Raymond and M. B. Francis, *J. Am. Chem. Soc.*, 2011, **133**, 14704–14709.
27 S. Aime, L. Calabi, C. Cavallotti, E. Gianolio, G. B. Giovenzana, P. Losi, A. Maiocchi, G. Palmisano and M. Sisti, *Inorg. Chem.*, 2004, **43**, 7588–7590.
28 N. Graeppi, D. H. Powell, G. Laurenczy, L. Zékány and A. Merbach, *Inorg. Chim. Acta*, 1995, **235**, 311–326.
29 R. Negri, F. Carniato, M. Botta, G. B. Giovenzana and L. Tei, *ChemPlusChem*, 2016, **81**, 235–241.
30 E. M. Gale, N. Kenton and P. Caravan, *MedChemComm*, 2013, **49**, 8060–8062.
31 A. Varga-Szemes, P. Kiss, A. Rab, P. Suranyi, Z. Lenkey, T. Simor, R. G. Bryant and G. A. Elgavish, *PLoS One*, 2016, **11**, e0149260.
32 C. Cossy, L. Helm and A. E. Merbach, *Inorg. Chem.*, 1988, **27**, 1973–1979.
33 C. Cossy, L. Helm and A. E. Merbach, *Inorg. Chem.*, 1989, **28**, 2699–2703.
34 S. Karimi and L. Helm, *Inorg. Chem.*, 2016, **55**, 4555–4563.
35 Z. Baranyai, D. D. Castelli, C. Platas-Iglesias, D. Esteban-Gomez, A. Bényei, L. Tei and M. Botta, *Inorg. Chem. Front.*, 2020, **7**, 795–803.
36 L. Leone, D. Esteban-Gómez, C. Platas-Iglesias, M. Milanesio and L. Tei, *MedChemComm*, 2019, **55**, 513–516.
37 B. Phukan, K. P. Malikidogo, C. S. Bonnet, É. Tóth, S. Mondal and C. Mukherjee, *ChemistrySelect*, 2018, **3**, 7668–7673.
38 S. Laus, R. Ruloff, É. Tóth and A. E. Merbach, *Chem. - Eur. J.*, 2003, **9**, 3555–3566.
39 P. Hermann, J. Kotek, V. Kubíček and I. Lukeš, *Dalton Trans.*, 2008, 3027–3047.
40 S. Aime, M. Botta, M. Fasano, M. P. M. Marques, C. F. Geraldes, D. Pubanz and A. E. Merbach, *Inorg. Chem.*, 1997, **36**, 2059–2068.
41 S. Laurent, L. V. Elst and R. N. Muller, *Contrast Media Mol. Imaging*, 2006, **1**, 128–137.
42 M. K. Thompson, M. Botta, G. Nicolle, L. Helm, S. Aime, A. E. Merbach and K. N. Raymond, *J. Am. Chem. Soc.*, 2003, **125**, 14274–14275.
43 Z. Baranyai, M. Botta, M. Fekete, G. B. Giovenzana, R. Negri, L. Tei and C. Platas-Iglesias, *Chem. - Eur. J.*, 2012, **18**, 7680–7685.
44 S. Aime, M. Botta, L. Frullano, S. Geninatti Crich, G. Giovenzana, R. Pagliarin, G. Palmisano, F. R. Sirtori and M. Sisti, *J. Med. Chem.*, 2000, **43**, 4017–4024.
45 P. Caravan, D. Esteban-Gómez, A. Rodríguez-Rodríguez and C. Platas-Iglesias, *Dalton Trans.*, 2019, **48**, 11161–11180.
46 A. Datta and K. N. Raymond, *Acc. Chem. Res.*, 2009, **42**, 938–947.
47 Y. Bretonnière, M. Mazzanti, J. Pécaut, F. A. Dunand and A. E. Merbach, *MedChemComm*, 2001, 621–622.

48 N. Chatterton, C. Gateau, M. Mazzanti, J. Pécaut, A. Borel, L. Helm and A. Merbach, *Dalton Trans.*, 2005, 1129–1135.
49 J. Peters, E. Zitha-Bovens, D. Corsi and C. Geraldes, *The Chemistry of Contrast Agents in Medical Magnetic Resonance Imaging*, John Wiley & Sons, 2001, p. 67.
50 A. Nonat, P. H. Fries, J. Pécaut and M. Mazzanti, *Chem. - Eur. J.*, 2007, **13**, 8489–8506.
51 B. Phukan, C. Mukherjee and R. Varshney, *Dalton Trans.*, 2018, **47**, 135–142.
52 M. Khannam, S. K. Sahoo and C. Mukherjee, *Eur. J. Inorg. Chem.*, 2019, **2019**, 2518–2523.
53 M. Regueiro-Figueroa and C. Platas-Iglesias, *J. Phys. Chem. A*, 2015, **119**, 6436–6445.
54 J. Tao, J. P. Perdew, V. N. Staroverov and G. E. Scuseria, *Phys. Rev. Lett.*, 2003, **91**, 146401.
55 M. J. Frisch, G. W. Trucks, H. B. Schlegel, G. E. Scuseria, M. A. Robb, J. R. Cheeseman, G. Scalmani, V. Barone, G. A. Petersson, H. Nakatsuji, X. Li, M. Caricato, A. V. Marenich, J. Bloino, B. G. Janesko, R. Gomperts, B. Mennucci, H. P. Hratchian, J. V. Ortiz, A. F. Izmaylov, J. L. Sonnenberg, D. Williams-Young, F. Ding, F. Lipparini, F. Egidi, J. Goings, B. Peng, A. Petrone, T. Henderson, D. Ranasinghe, V. G. Zakrzewski, J. Gao, N. Rega, G. Zheng, W. Liang, M. Hada, M. Ehara, K. Toyota, R. Fukuda, J. Hasegawa, M. Ishida, T. Nakajima, Y. Honda, O. Kitao, H. Nakai, T. Vreven, K. Throssell, J. A. Montgomery Jr, J. E. Peralta, F. Ogliaro, M. J. Bearpark, J. J. Heyd, E. N. Brothers, K. N. Kudin, V. N. Staroverov, T. A. Keith, R. Kobayashi, J. Normand, K. Raghavachari, A. P. Rendell, J. C. Burant, S. S. Iyengar, J. Tomasi, M. Cossi, J. M. Millam, M. Klene, C. Adamo, R. Cammi, J. W. Ochterski, R. L. Martin, K. Morokuma, O. Farkas, J. B. Foresman and D. J. Fox, *Gaussian – 16 Revision C.01*, Gaussian Inc., Wallingford CT, 2016.
56 A. Roca-Sabio, M. Regueiro-Figueroa, D. Esteban-Gómez, A. de Blas, T. Rodríguez-Blas and C. Platas-Iglesias, *Comput. Theor. Chem.*, 2012, **999**, 93–104.
57 M. Dolg and H. Stoll, *Theor. Chim. Acta*, 1989, **75**, 173–194.
58 M. Dolg, H. Stoll and H. Preuss, *J. Chem. Phys.*, 1989, **90**, 1730–1734.
59 A. Grüneis, M. Marsman and G. Kresse, *J. Chem. Phys.*, 2010, **133**, 074107.
60 M. Dolg and X. Cao, *Chem. Rev.*, 2012, **112**, 403–480.
61 M. Dolg and H. Stoll, *Theor. Chim. Acta*, 1989, **75**, 369–387.
62 A. Weigand, X. Cao, J. Yang and M. Dolg, *Theor. Chem. Acc.*, 2010, **126**, 117–127.
63 U. Cosentino, A. Villa, D. Pitea, G. Moro, V. Barone and A. Maiocchi, *J. Am. Chem. Soc.*, 2002, **124**, 4901–4909.
64 R. O. Freire, G. B. Rocha and A. M. Simas, *J. Mol. Model.*, 2006, **12**, 373–389.
65 L. Maron and O. Eisenstein, *J. Phys. Chem. A*, 2000, **104**, 7140–7143.
66 D. Guillaumont, *J. Phys. Chem. A*, 2004, **108**, 6893–6900.
67 J. Tomasi, B. Mennucci and R. Cammi, *Chem. Rev.*, 2005, **105**, 2999–3094.
68 M. Cossi, V. Barone, R. Cammi and J. Tomasi, *Chem. Phys. Lett.*, 1996, **255**, 327–335.
69 D. Esteban-Gómez, A. De Blas, T. Rodríguez-Blas, L. Helm and C. Platas-Iglesias, *ChemPhysChem*, 2012, **13**, 3640–3650.
70 A. Zawada, R. W. Gora, M. M. Mikołajczyk and W. Bartkowiak, *J. Phys. Chem. A*, 2012, **116**, 4409–4416.
71 A. K. Rappé, C. J. Casewit, K. Colwell, W. A. Goddard III and W. M. Skiff, *J. Am. Chem. Soc.*, 1992, **114**, 10024–10035.
72 A. V. Marenich, C. J. Cramer and D. G. Truhlar, *J. Phys. Chem. B*, 2009, **113**, 6378–6396.
73 Y. Zhao and D. G. Truhlar, *Theor. Chem. Acc.*, 2008, **120**, 215–241.
74 C. F. Matta and R. J. Boyd, *The quantum theory of atoms in molecules: from solid state to DNA and drug design*, 2007.
75 T. Lu and F. Chen, *J. Comput. Chem.*, 2012, **33**, 580–592.
76 M. P. Mitoraj, A. Michalak and T. Ziegler, *J. Chem. Theory Comput.*, 2009, **5**, 962–975.
77 C. Van Wüllen, *J. Comput. Chem.*, 1999, **20**, 51–62.
78 E. v. Lenthe, E.-J. Baerends and J. G. Snijders, *J. Chem. Phys.*, 1993, **99**, 4597–4610.
79 E. van Lenthe, E.-J. Baerends and J. G. Snijders, *J. Chem. Phys.*, 1994, **101**, 9783–9792.
80 D. A. Pantazis and F. Neese, *J. Chem. Theory Comput.*, 2009, **5**, 2229–2238.
81 G. t. Te Velde, F. M. Bickelhaupt, E. J. Baerends, C. Fonseca Guerra, S. J. van Gisbergen, J. G. Snijders and T. Ziegler, *J. Comput. Chem.*, 2001, **22**, 931–967.
82 E. Van Lenthe and E. J. Baerends, *J. Comput. Chem.*, 2003, **24**, 1142–1156.
83 A. D. Becke, *Phys. Rev. A*, 1988, **38**, 3098.
84 J. P. Perdew, *Phys. Rev. B*, 1986, **33**, 8822.
85 X. Yang, C. P. Burns, M. Nippe and M. B. Hall, *Inorg. Chem.*, 2021, **60**, 9394–9401.
86 F. Neese, *Wiley Interdiscip. Rev.: Comput. Mol. Sci.*, 2012, **2**, 73–78.
87 D. Aravena, F. Neese and D. A. Pantazis, *J. Chem. Theory Comput.*, 2016, **12**, 1148–1156.
88 S. R. Gadre and R. N. Shirsat, *Electrostatics of atoms and molecules*, Universities Press, 2000.
89 P. V. Bijina and C. H. Suresh, *J. Chem. Sci.*, 2016, **128**, 1677–1686.
90 S. F. Boys and F. Bernardi, *Mol. Phys.*, 1970, **19**, 553–566.
91 R. Gulde, P. Pollak and F. Weigend, *J. Chem. Theory Comput.*, 2012, **8**, 4062–4068.
92 M. Regueiro-Figueroa, D. Esteban-Gómez, A. de Blas, T. Rodríguez-Blas and C. Platas-Iglesias, *Chem. - Eur. J.*, 2014, **20**, 3974–3981.
93 D. Esteban-Gómez, C. Cassino, M. Botta and C. Platas-Iglesias, *RSC Adv.*, 2014, **4**, 7094–7103.
94 V. Patinec, G. A. Rolla, M. Botta, R. Tripier, D. Esteban-Gómez and C. Platas-Iglesias, *Inorg. Chem.*, 2013, **52**, 11173–11184.
95 A. M. Nonat, C. Gateau, P. H. Fries, L. Helm and M. Mazzanti, *Eur. J. Inorg. Chem.*, 2012, **2012**, 2049–2061.
96 P. W. Ayers, R. G. Parr and R. G. Pearson, *J. Chem. Phys.*, 2006, **124**, 194107–194116.
97 J. Zhang and M. Dolg, *J. Phys. Chem. A*, 2015, **119**, 774–780.

98 K. Pota, Z. Garda, F. K. Kálmán, J. L. Barriada, D. Esteban-Gómez, C. Platas-Iglesias, I. Tóth, E. Brücher and G. Tircsó, *New J. Chem.*, 2018, **42**, 8001–8011.
99 O. V. Yazyev, L. Helm, V. G. Malkin and O. L. Malkina, *J. Phys. Chem. A*, 2005, **109**, 10997–11005.
100 O. V. Yazyev and L. Helm, *Eur. J. Inorg. Chem.*, 2008, **2008**, 201–211.
101 R. Pollet, N. N. Nair and D. Marx, *Inorg. Chem.*, 2011, **50**, 4791–4797.
102 G. I. Csonka, J. P. Perdew and A. Ruzsinszky, *J. Chem. Theory Comput.*, 2010, **6**, 3688–3703.
103 X. Jin, Z. Qian, B. Lu and S. Bi, *Dalton Trans.*, 2011, **40**, 567–572.
104 A. S. Merbach, L. Helm and E. Toth, *The chemistry of contrast agents in medical magnetic resonance imaging*, John Wiley & Sons, 2013.
105 R. Pujales-Paradela, F. Carniato, D. Esteban-Gómez, M. Botta and C. Platas-Iglesias, *Dalton Trans.*, 2019, **48**, 3962–3972.
106 L. Leone, S. Camorali, A. Freire-García, C. Platas-Iglesias, D. E. Gomez and L. Tei, *Dalton Trans.*, 2021, **50**, 5506–5518.
107 A. D. Becke and K. E. Edgecombe, *J. Chem. Phys.*, 1990, **92**, 5397–5403.
108 F. M. Bickelhaupt and E. J. Baerends, *Rev. Comput. Chem.*, 2000, 1–86.
109 E. M. Lopez-Vidal, M. Regueiro-Figueroa, M. D. García, C. Platas-Iglesias, C. Peinador and J. M. Quintela, *Inorg. Chem.*, 2012, **51**, 4429–4431.